Sparsity-based three-dimensional image reconstruction for near-field MIMO radar imaging

Figen S. OKTEM[*]
Department of Electrical and Electronics Engineering, Faculty of Engineering, Middle East Technical University,
Ankara, Turkey

Abstract: Near-field multiple-input multiple-output (MIMO) radar imaging systems are of interest in diverse fields such as medicine, through-wall imaging, airport security, concealed weapon detection, and surveillance. The successful operation of these radar imaging systems highly depends on the quality of the images reconstructed from radar data. Since the underlying scenes can be typically represented sparsely in some transform domain, sparsity priors can effectively regularize the image formation problem and hence enable high-quality reconstructions. In this paper, we develop an efficient three-dimensional image reconstruction method that exploits sparsity in near-field MIMO radar imaging. Sparsity is enforced using total variation regularization, and the reflectivity distribution is reconstructed iteratively without requiring computation with huge matrices. The performance of the developed algorithm is illustrated through numerical simulations. The results demonstrate the effectiveness of the sparsity-based method compared to a classical image reconstruction method in terms of image quality.

Key words: Inverse problems, sparse reconstruction, image reconstruction, multiple-input multiple-output radar imaging, microwave imaging

1. Introduction

Near-field radar imaging systems are of interest in various fields including medical diagnosis, through-wall imaging, airport security, concealed weapon detection, and surveillance [1–4]. Many of the earlier developed systems operate in monostatic mode, i.e. with colocated transmitter and receiver antennas [5–9]. However, recently there has been growing interest in using sparse multiple-input multiple-output (MIMO) arrays with spatially distributed transmit and receive antennas (i.e. multistatic array) because these can offer high resolution with reduced hardware complexity, cost, and acquisition time [10–14].

The successful operation of near-field radar imaging systems highly depends on the quality of the images reconstructed using radar data. The classical approaches used for reconstructing the three-dimensional scene reflectivity distribution are direct inversion methods such as backprojection and Kirchhoff migration algorithms [15–21]. Although these classical methods generally offer fast computation, the reconstruction performance degrades substantially in the presence of limited data (as acquired with sparse arrays) and measurement noise.

Motivated by compressed sensing theory [22], sparsity-based reconstruction provides state-of-the-art image reconstruction quality in various radar imaging problems with limited data [23–26]. For sparsity-based

─────────────────
[*]Correspondence: figeno@metu.edu.tr

reconstruction, there are various publicly available algorithms [27], but they are mostly for the recovery of two-dimensional and real-valued images. Moreover, when handling large-dimensional imaging problems, these algorithms are highly inefficient in terms of both computation time and memory usage because they involve computation with huge matrices. These limitations require the adaptation of the sparse recovery techniques to a particular problem at hand. Most of the adapted sparse reconstruction techniques for radar imaging are for monostatic or far-field imaging settings [6–9, 23, 28–36]. On the other hand, there is limited work for multistatic and near-field settings [37–39], all of which are specialized to a particular application.

In this paper, we develop an efficient sparsity-based method to reconstruct the three-dimensional complex-valued reflectivity distribution in a general near-field MIMO radar imaging setting. Sparsity is enforced in a three-dimensional transform domain using total variation regularization, and the reconstruction is performed iteratively without requiring computation with huge matrices. The developed sparse recovery algorithm is a special case of the "half-quadratic regularization" approach [40, 41], which solves a series of quadratic problems to obtain the reconstruction. Numerical simulations are performed for a microwave imaging setting with a sparse MIMO array. The effectiveness of the developed method is demonstrated by comparing the performance with the classical backprojection method.

The paper is organized as follows. In Section 2, we introduce the general measurement model for a near-field and multistatic radar imaging setting. The image formation problem is formulated as an inverse problem in Section 3. Section 4 presents the developed sparsity-based reconstruction method for efficiently solving the resulting inverse problem. Numerical simulation results are presented in Section 5 for a microwave imaging application with a sparse MIMO array. Section 6 concludes the paper.

2. Forward problem

The first task in solving the imaging problem is to mathematically relate the unknown reflectivity field of the scene to the radar measurements. The observation geometry for near-field MIMO imaging is illustrated in Figure 1. The transmit and receive antennas are spatially distributed on a planar MIMO array located at $z = 0$. Each transmit antenna, located at $(x_t, y_t, 0)$, illuminates a scene that lies in the near-field of the array. Under Born approximation, the radar pulses captured by the receive antenna at $(x_r, y_r, 0)$ can be expressed in the time-domain as follows [16]:

$$r(x_t, y_t, x_r, y_r, t) = \iiint \frac{1}{4\pi d_t d_r} s(x, y, z) \, p\left(t - \frac{d_t}{c} - \frac{d_r}{c}\right) dx \, dy \, dz, \tag{1}$$

where

$$d_t = \sqrt{(x_t - x)^2 + (y_t - y)^2 + z^2}, \tag{2}$$

$$d_r = \sqrt{(x_r - x)^2 + (y_r - y)^2 + z^2}. \tag{3}$$

Here $r(x_t, y_t, x_r, y_r, t)$ denotes the time-domain measurement obtained using the transmitter at $(x_t, y_t, 0)$ and the receiver at $(x_r, y_r, 0)$. Moreover, $s(x, y, z)$ is the complex-valued three-dimensional reflectivity distribution of the scene, d_t and d_r respectively denote the distances from the corresponding transmit and receive antenna elements to the scatterer at (x, y, z), $p(t)$ is the transmitted pulse, and c denotes the speed of the light.
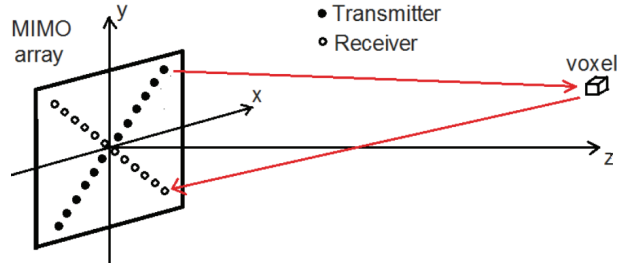
Figure 1. Near-field MIMO radar imaging system.

By applying Fourier transform, the measurement model can also be expressed in the temporal frequency domain [16] as:

$$r(x_t, z_t, x_r, z_r, k) = \int\int\int \frac{1}{4\pi d_t d_r} s(x, y, z) \, p(k) \, e^{-jkd_t} \, e^{-jkd_r} dx \, dy \, dz. \tag{4}$$

Here $p(k)$ denotes the Fourier transform of the transmitted signal, where $k = 2\pi f/c$ denotes the frequency-wavenumber and f denotes the temporal frequency.

Because the measurements will be acquired digitally and image reconstruction will be performed on a computer, a discrete forward model is needed. The continuous forward model in Eq. (1) or Eq. (4) is converted to a discrete model by replacing the three-dimensional continuous reflectivity function with its discrete representation in terms of voxels. By using lexicographic ordering, the voxel values of the discretized reflectivity function are put into the vector $s \in C^N$. The measurement vector is also denoted by $y \in C^M$, which contains the discrete set of measurements obtained using different transmitter-receiver pairs and frequency steps. Then the linear relation between the image vector s and the measurement vector y can be expressed as follows:

$$y = As, \tag{5}$$

where $A \in C^{M \times N}$ is the observation matrix. In general, the observation matrix A is rectangular. The total number of rows in A is the length, M, of the measurement vector, which is equal to the multiplication of the number of transmit and receive antennas, and used frequency steps. The number of columns in A is equal to the number of voxels, N.

Using the frequency-domain model given in Eq. (4), the (m, n)th element of the observation matrix, representing the contribution of the nth voxel to the mth measurement, can be obtained [42] as:

$$A_{m,n} = \frac{p(k_m)e^{-jk_m d_{t_m}^{(n)}} e^{-jk_m d_{r_m}^{(n)}}}{4\pi d_{t_m}^{(n)} d_{r_m}^{(n)}}. \tag{6}$$

Here the measurement index m indicates the locations of the transmitting and receiving antennas, as well as the frequency, k_m, used in this measurement. Moreover, $d_{t_m}^{(n)}$ and $d_{r_m}^{(n)}$ respectively represent the distances from the center of the nth voxel to the transmitter and receiver used in the mth measurement. Note that, for the reflectivity function, the voxel size is chosen based on the desired down-range and cross-range resolutions of the MIMO imaging system.

3. Inverse problem

In the inverse problem, the goal is to estimate the three-dimensional complex-valued reflectivity field, s, of the scene from the radar measurements, y. Because the reflectivity field generally has strong correlations along

range and cross-range directions, it can be sparsely represented in some transform domain. Incorporation of such sparsity priors helps to regularize the imaging problem and hence prevents the reconstruction artifacts that would otherwise result from reduced and noisy data.

To enforce sparsity [27, 43, 44], the inverse problem is formulated as:

$$\min_{s} \ \|y - As\|_2 + \alpha^2 \|\Phi s\|_1, \tag{7}$$

where Φ is a sparsifying transform operator for s, chosen based on the reflectivity characteristics of the scene, and α is the regularization parameter. For example, if the scene consists of point scatterers, the identity operator can be chosen (i.e. $\Phi = I$) to enforce sparsity in the space domain. For extended targets, a commonly used choice for Φ is the discrete gradient operator, which can be expressed for the three-dimensional reflectivity image as:

$$\Phi = \begin{bmatrix} D_x \\ D_y \\ D_z \end{bmatrix}, \tag{8}$$

where the matrices D_x, D_y, and D_z represent discrete approximations to the gradient operator along the x, y, and z directions, respectively. This regularization choice is also known as total variation and allows to preserve sharp edges and rapidly changing structures in an extended target when they fit the data. In practice, there is no need to form the matrices D_x, D_y, and D_z since these operations can be efficiently computed by filtering the three-dimensional reflectivity image with simple derivative kernels, such as $[-1 \ 0 \ 1]$, along the respective coordinate directions.

4. Image reconstruction algorithm

Because there is no closed-form solution for the resulting convex optimization problem in Eq. (7), numerical techniques are needed to find the solution. Various algorithmic approaches with different convergence rates and guarantees exist for solving such optimization problems. An important class of algorithms is gradient-based algorithms, which are commonly obtained with a fixed-point approach applied to an approximated problem [27, 43, 44]. To efficiently obtain the solution, here we use such a fixed-point iterative approach [41] based on the half-quadratic regularization method [40].

To develop the algorithm, first, a smooth approximation is applied to the l_1-norm to make it differentiable everywhere, which results in the following optimization problem [41]:

$$\min_{s} \ \|y - As\|_2 + \alpha^2 \sum_{i=1}^{3N} \sqrt{|[\Phi s]_i|^2 + \beta}. \tag{9}$$

Here β is the smoothing parameter. Note that when $\beta = 0$, the above cost function reduces to the original cost function in Eq. (7). Moreover, when β is sufficiently small, it provides a differentiable cost function that is close to the original one. By differentiating this new cost function with respect to s and equating it to zero, the following nonlinear equation can be obtained for the solution:

$$\left(A^H A + \alpha^2 \Phi^H W(s)\Phi\right) s = A^H y, \tag{10}$$

where $W(s)$ is a matrix that depends on the unknown s as follows:

$$W(s) = diag\left(\frac{1/2}{\sqrt{|[\Phi s]_i|^2 + \beta}}\right).$$ (11)

Based on this result, a fixed-point iteration is obtained, which successively computes the matrix $W(s)$ using Eq. (11) and then updates the solution s by solving a linear system. The computations in the lth iteration can then be summarized as follows:

$$W(s_l) = diag\left(\frac{1/2}{\sqrt{|[\Phi s_l]_i|^2 + \beta}}\right),$$ (12)

$$s_{l+1} = \left(A^H A + \alpha^2 \Phi^H W(s_l)\Phi\right)^{-1} A^H y.$$ (13)

The iteration in Eq. (13) computes the solution of the linear system in Eq. (10) with a direct matrix inversion approach. However, for the reconstruction of large-scale images, such a direct approach is not feasible since it requires working with huge matrices. As a result, in practice, more efficient iterative methods must be employed for the solution of the resulting sets of equations. Here the conjugate gradient (CG) method is adapted to efficiently solve this linear system. The iterations of the CG algorithm are performed efficiently using only scalar products of vectors and evaluations of the forward operator and its adjoint (i.e. Ax and $A^H y$) for different inputs. This eliminates the need to explicitly form the matrix $B = A^H A + \alpha^2 \Phi^H W(s_k)\Phi$ or its inverse.

While sparsity-based reconstruction enables better image quality, it generally requires a much higher computational cost than the direct inversion methods such as backprojection. The computational complexity of the fixed-point approach presented here is mainly dominated by the evaluations of the forward and adjoint operators (i.e. Ax and $A^H y$) in the inner CG iterations. For example, if the number of inner CG iterations is denoted by L_i, and the number of outer iterations is denoted by L_o, then the number of forward and adjoint operator computations required is $L_o \times L_i$. On the other hand, only a single adjoint operator evaluation is required for the backprojection method. As a result, the direct inversion methods like backprojection are generally three to four orders of magnitude faster than the sparsity-based reconstruction approach presented here.

5. Numerical results

In this section, we illustrate the performance of sparsity-based image reconstruction for an application in microwave imaging [16]. For this, we consider the sparse MIMO array topology shown in Figure 2, which is known as the Mills Cross array. The width of the planar array is 0.3 m, and 12 transmit and 13 receive antennas are spaced uniformly along its diagonals in a cross configuration. The number of frequency steps is chosen as 21, ranging from 4 to 16 GHz, with a step of 0.6 GHz. The target center is located at a distance of 0.5 m from the MIMO array.

For such an imaging setting, the expected theoretical resolution [16] with a nonsparse array is 2.5 cm in the cross-range directions, x and y, and 1.25 cm in the down-range direction, z. The goal is to estimate the reflectivity image within a cube of size 0.3 m × 0.3 m × 0.3 m, where the voxel size is chosen as 1.25 cm × 1.25 cm × 0.625 cm (i.e. half of the expected resolution in each direction). Note that the underlying image

reconstruction problem is highly underdetermined; the ratio of the number of measurements to the number of unknown image voxels is nearly 10 percent.
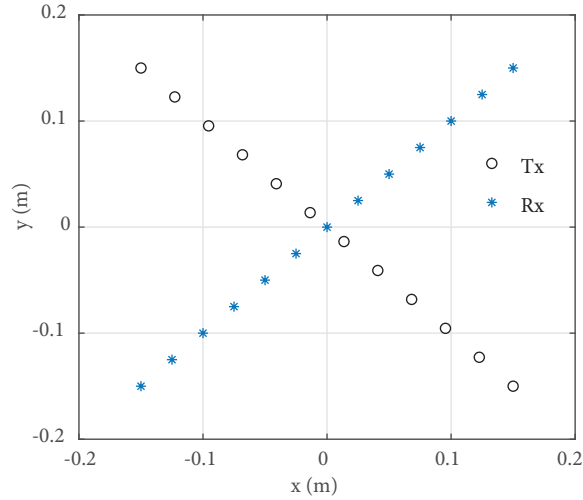

**Figure 2**. 2D MIMO array with 12 transmit and 13 receive antennas arranged in a cross configuration.

Two different target scenarios are considered in the numerical simulations. The first scenario is the same as the one in [16], where the scene consists of nine point scatterers located within a volume of size 0.2 m × 0.2 m × 0.15 m. The left column of Figure 3 shows different views of the true reflectivity image for this target scenario. The radar measurements are simulated using the model in Eq. (5), and then the 3D reflectivity image is reconstructed from the radar measurements using the developed sparsity-enforcing algorithm with regularization parameter $\alpha = 25$. The conventional backprojection algorithm is also implemented in the frequency-domain for comparison. The reconstructions obtained with the classical backprojection algorithm and sparsity-enforcing algorithm are respectively shown in the middle and right columns of Figure 3. The figure contains the summed magnitude of the 3D images along range direction z and cross-range direction x, as well as the three slices at $z = 0.425$ m, $z = 0.5$ m, and $z = 0.575$ m, containing the point scatterers.

The results demonstrate the superior focusing capability of the developed imaging algorithm compared to the classical backprojection method. The theoretical resolution is achieved even though the acquired data are substantially reduced due to the use of a sparse array and few frequency steps. Such high resolution is not possible to be achieved with the backprojection algorithm both in the range and cross-range directions. Moreover, as can be seen from the second row of Figure 3, the neighboring range slices that do not contain point scatterers are almost perfectly clean in our reconstructions, while this is not true for the backprojection result. The summed magnitude and the slice at $z = 0.575$ m are replotted in Figure 4 together with their mesh plots for better visualization. Because the same target scenario as in [16] is considered here, one can additionally compare the proposed approach with the range migration method developed in [16], which requires a uniform array topology. A uniform array of similar size is used there with many more antenna elements and frequency steps, which results in 1000 times more measurements than in our case. Visual inspection of the results presented in that work illustrates that sparsity-based reconstruction also provides better image quality than the range migration technique, even with significantly fewer measurements.

To quantitatively evaluate the quality of the reconstructions, the peak signal-to-noise-ratios (PSNRs) are also calculated, which are 23.18 dB and 46.38 dB for the backprojection and the sparsity-based reconstructions,
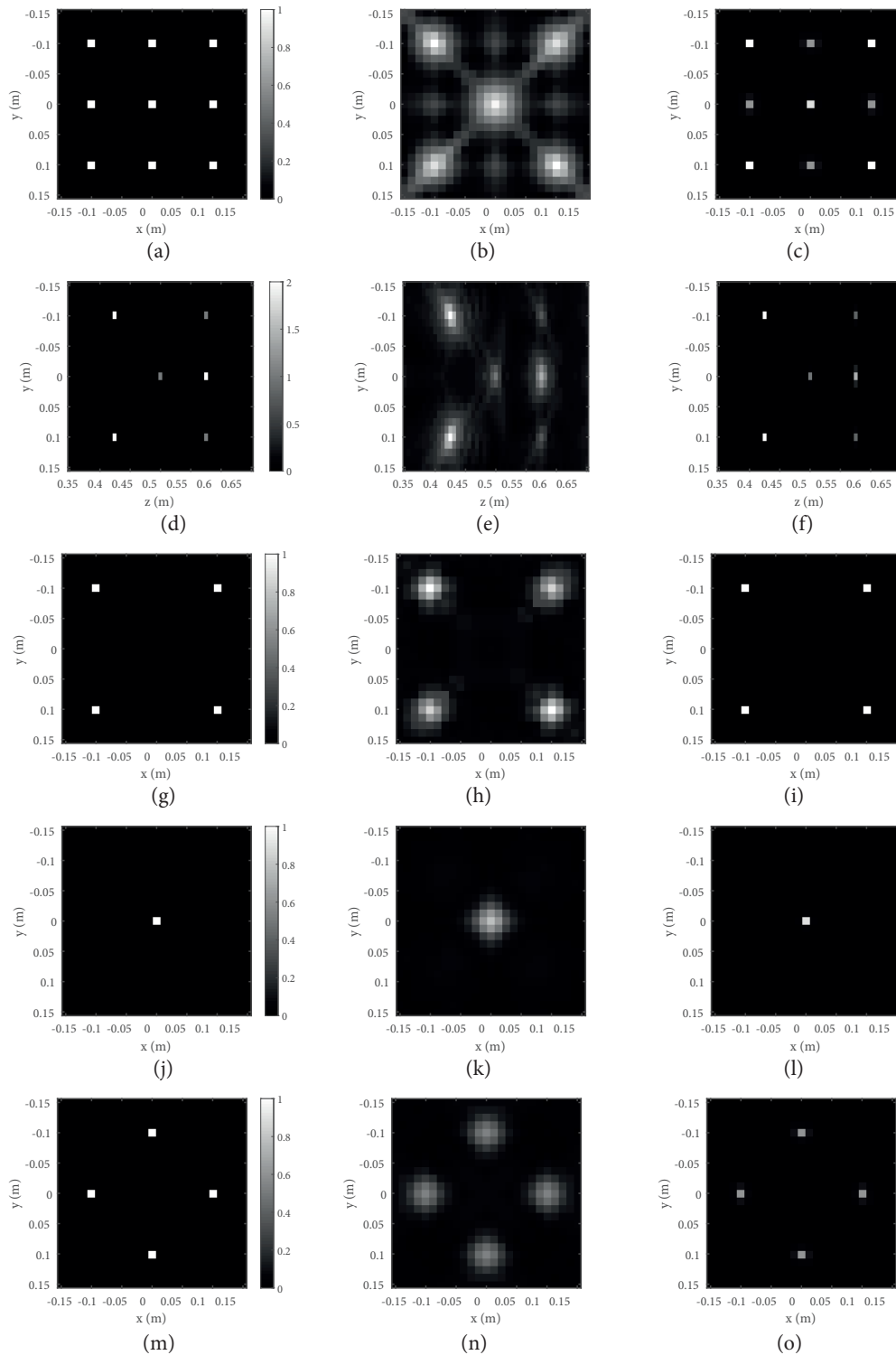
Figure 3. Imaging results for the first target scenario with nine distributed point scatterers. The left, middle, and right columns respectively show different views of the true reflectivity image, backprojection reconstruction, and sparsity-based reconstruction. Each 3D reconstruction is normalized by the largest magnitude value, and figures in the same row share the same color bar. The first and second rows respectively show the summed magnitude of the 3D images along the range direction z and the cross-range direction x. The third, fourth, and fifth rows respectively show the magnitude slices at $z = 0.425$ m, $z = 0.5$ m, and $z = 0.575$ m.
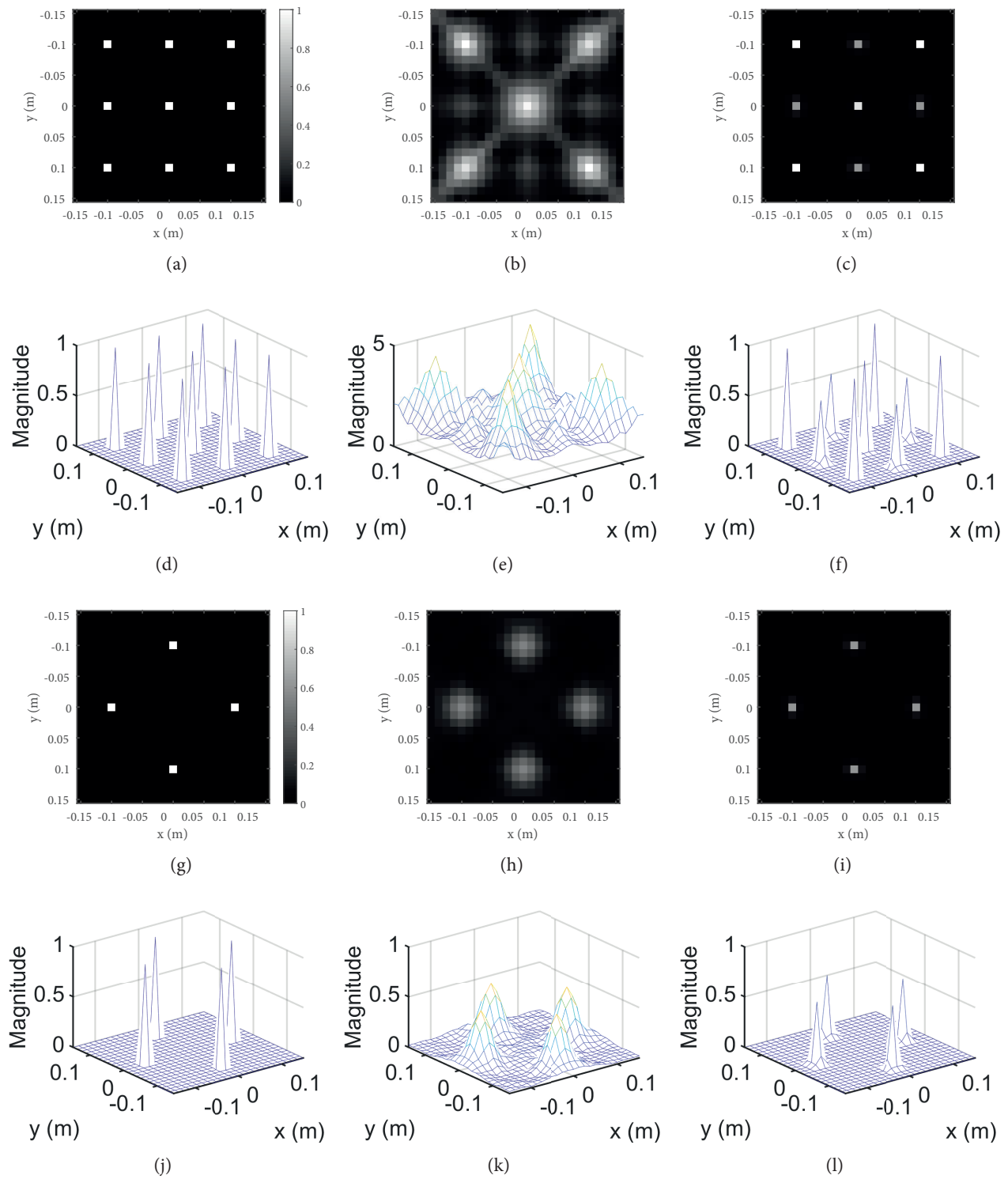
Figure 4. Imaging results for the first target scenario with nine distributed point scatterers. The summed magnitudes (a–f) and the slices at $z = 0.575$ m (g–l) are replotted together with their mesh plots for better visualization.

respectively. A higher value of PSNR generally indicates that the image quality is better. The difference in these PSNR values also demonstrates the effectiveness of the sparsity-based reconstruction. In computational image formation, typical values for the PSNR are between 20 and 40 dB, where 40 dB or higher PSNR roughly corresponds to excellent image quality and PSNRs lower than 20 dB indicate poor image quality. Hence, these PSNR values also suggest that, for simple point scatterers, the quality of the sparsity-based reconstruction is almost excellent, while backprojection only provides a reconstruction of average quality.

In the second numerical simulation, imaging of a distributed target is analyzed. The target contains a box of size 0.1 m × 0.1 m × 0.1 m with a uniform reflectivity value of 0.5, and the letter U, which has twice the reflectivity, is inside the box. The left column of Figure 5 provides different views of the true reflectivity image for this scenario. The radar measurements are again simulated using the model in Eq. (5), and then the 3D reflectivity image is reconstructed using the developed sparsity-enforcing algorithm with the regularization parameter $\alpha = 25$. The reconstructions obtained with the classical backprojection algorithm and the sparsity-enforcing algorithm are shown in the middle and right columns of Figure 5, respectively. The figure shows the summed magnitude of each 3D image along range direction z and cross-range direction x, as well as the three central slices at $z = 0.48125$ m, $z = 0.49375$ m, and $z = 0.50625$ m, containing the uniform box with and without the letter U.

The results for the distributed target also demonstrate the superior focusing performance of the developed algorithm compared to the classical backprojection method. In fact, in this case, the characteristics of the target are not reconstructed well with the backprojection algorithm as can be seen from the middle column of Figure 5. In particular, the shape of the box and the letter U are not clearly visible in the corresponding slices. On the other hand, the sparsity-based algorithm is capable of reconstructing the fine details with the provided limited data, as can be clearly seen from the slices given in the right column of Figure 5. The summed magnitude and the slice at $z = 0.50625$ m are replotted in Figure 6 together with their mesh plots for better visualization.

The PSNR values also support these observations since the PSNRs of the backprojection and sparsity-based reconstructions are 11.34 dB and 24.15 dB, respectively. These PSNR values also indicate that the backprojection result does not have acceptable image quality, while sparsity-based reconstruction has good quality, although not perfect. However, considering the limited amount of measurements available and the complexity of the distributed target, the sparsity-based reconstruction can be regarded as successful.

6. Conclusion

In summary, we have presented an efficient sparsity-based image reconstruction method for near-field MIMO radar imaging. Because the three-dimensional scene reflectivity has correlations along both range and cross-range directions, a sparse representation model is exploited for reconstruction with limited data. The developed sparse recovery algorithm, which is a special case of the "half-quadratic regularization" method, performs the reconstruction efficiently without requiring computation with huge matrices. The simulation results have demonstrated the superior focusing capability of the developed reconstruction method compared to the classical backprojection method for an imaging setting with limited data. The results suggest that high-quality images can be obtained with the developed sparsity-based method even with sparse MIMO arrays and sparse frequency data.

Acknowledgment
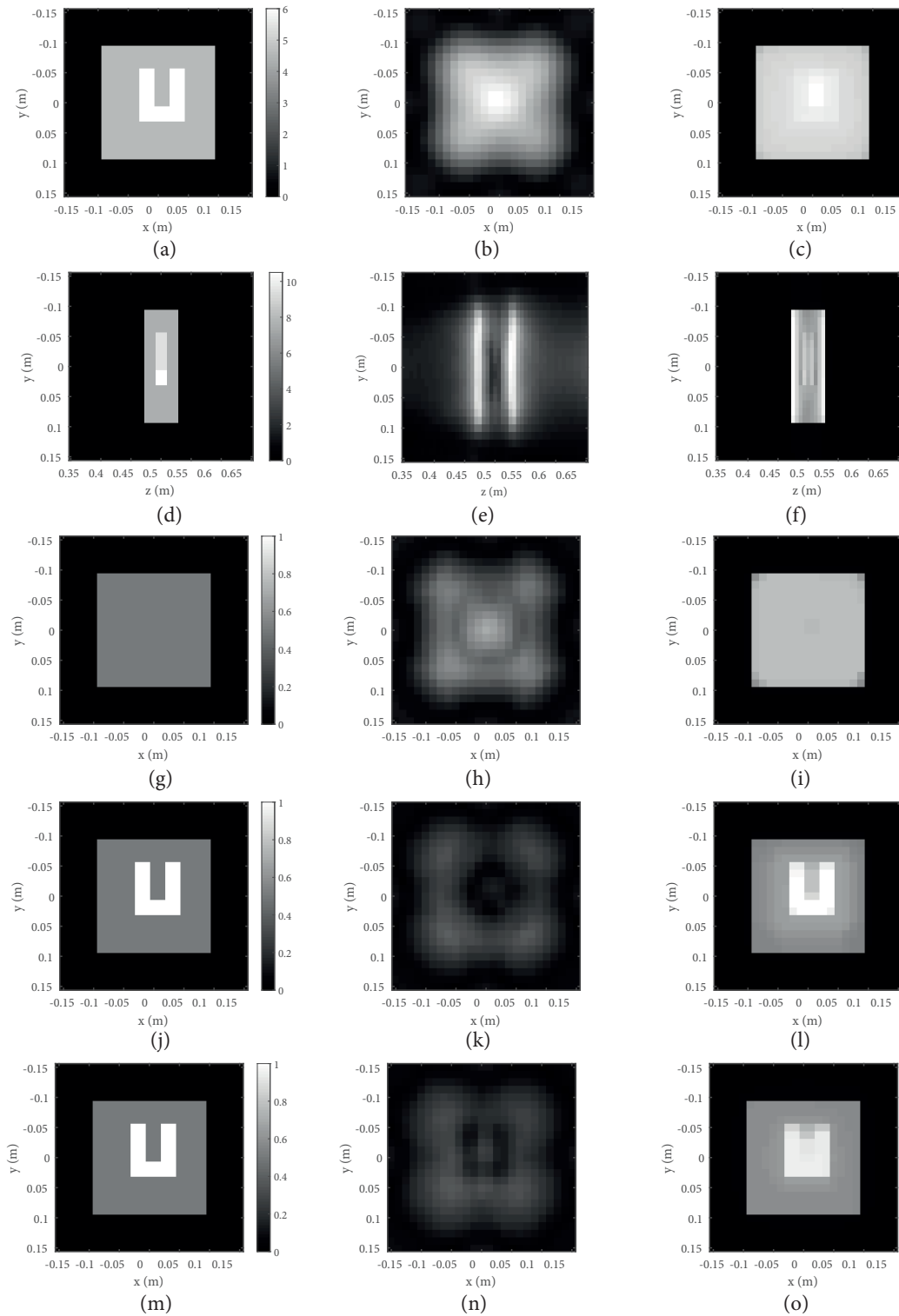
Figure 5. Imaging results for the second scenario with a distributed target. The left, middle, and right columns respectively show different views of the true reflectivity image, backprojection reconstruction, and sparsity-based reconstruction. Each 3D reconstruction is normalized by the largest magnitude value, and figures in the same row share the same color bar. The first and second rows respectively show the summed magnitude of the 3D images along the range direction z and the cross-range direction x. The third, fourth, and fifth rows respectively show the magnitude slices at $z = 0.48125$ m, $z = 0.49375$ m, and $z = 0.50625$ m.

(a)

(b)

(c)

(d)

(e)

(f)

(g)

(h)

(i)

(j)

(k)

(l)
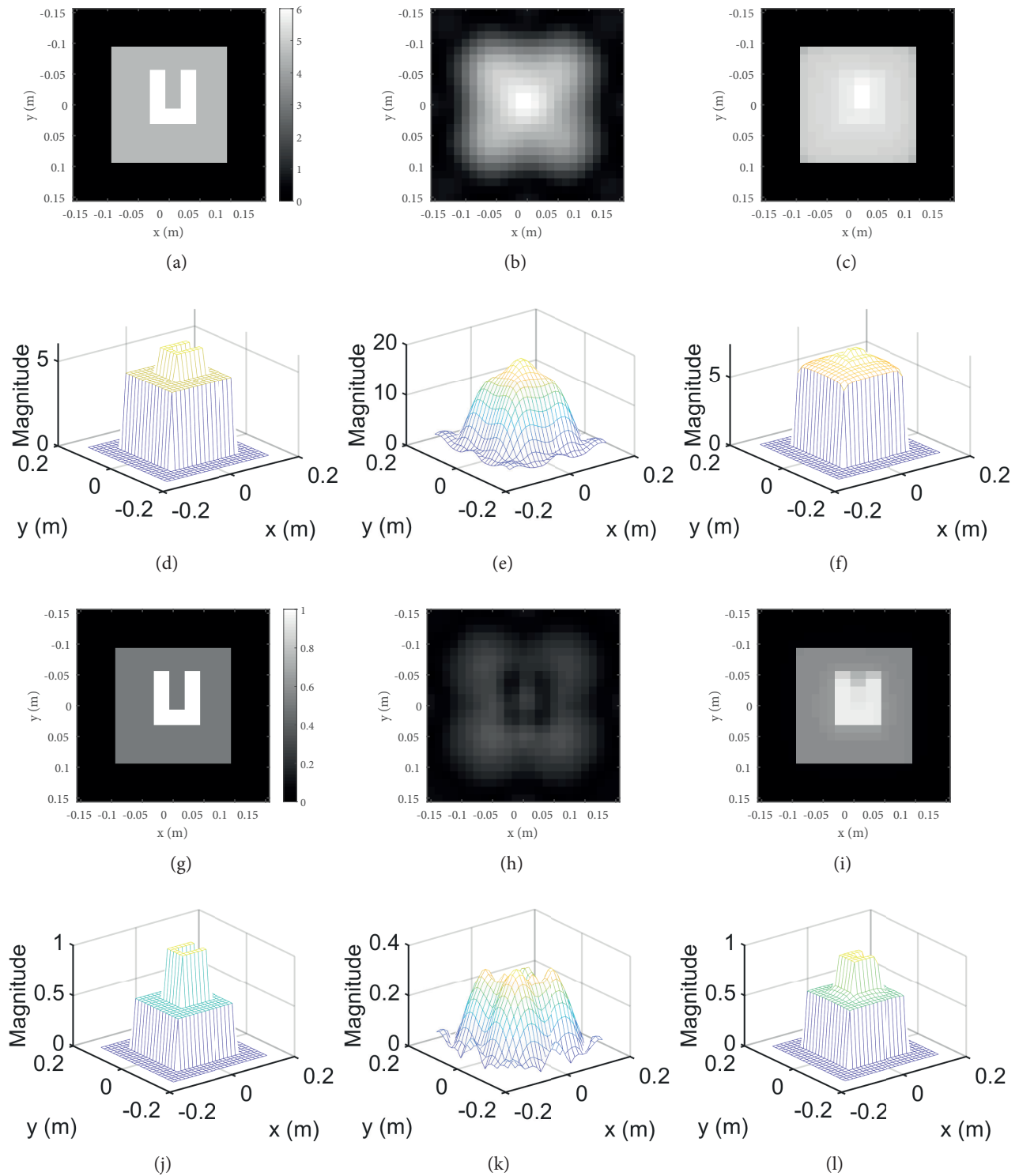
Figure 6. Imaging results for the second scenario with a distributed target. The summed magnitudes (a–f) and the slices at $z = 0.50625$ m (g–l) are replotted together with their mesh plots for better visualization.

References

[1] Yarovoy AG, Savelyev TG, Aubry PJ, Lys PE, Ligthart LP. UWB array-based sensor for near-field imaging. IEEE Trans on Microwave Theory and Techniques 2007; 55 (6): 1288–1295.

[2] Zhuge X, Yarovoy AG. A sparse aperture MIMO-SAR-based UWB imaging system for concealed weapon detection. IEEE Transactions on Geoscience and Remote Sensing 2011; 49 (1): 509-518.

[3] Ahmed SS, Schiessl A, Gumbmann F, Tiebout M, Methfessel S et al. Advanced microwave imaging. IEEE Microwave Magazine 2012; 13 (6): 26-43.

[4] Zhou Y, Yu J, Xu Z, Wang Y, Cao Q. Fast modeling methods for estimating imaging performance of whole body screening. IEEE Antennas and Wireless Propagation Letters 2019; 18 (1): 39-43.

[5] Sheen DM, McMakin DL, Hall TE. Three-dimensional millimeter-wave imaging for concealed weapon detection. IEEE Transactions on Microwave Theory and Techniques 2001; 49 (9): 1581-1592.

[6] Li S, Zhao G, Li H, Ren B, Hu W et al. Near-field radar imaging via compressive sensing. IEEE Transactions on Antennas and Propagation 2015; 63 (2): 828-833.

[7] Wei SJ, Zhang XL, Shi J, Liao KF. Sparse array microwave 3-D imaging: compressed sensing recovery and experimental study. Progress in Electromagnetics Research 2013; 135: 161-181.

[8] Yiğit E. Compressed sensing for millimeter-wave ground based SAR/ISAR imaging. Journal of Infrared, Millimeter, and Terahertz Waves 2014; 35 (11): 932-948.

[9] Zhao G, Li S, Ren B, Qiu Q, Sun H. Cylindrical three-dimensional millimeter-wave imaging via compressive sensing. International Journal of Antennas and Propagation 2015; 2015: 218751.

[10] Ahmed SS, Schiessl A, Schmidt LP. A novel fully electronic active real-time imager based on a planar multistatic sparse array. IEEE Transactions on Microwave Theory and Techniques 2011; 59 (12): 3567-3576.

[11] Zhuge X, Yarovoy AG. Sparse multiple-input multiple-output arrays for high-resolution near-field ultra-wideband imaging. IET Microwaves, Antennas & Propagation 2011; 5 (13): 1552-1562.

[12] Tan K, Wu S, Wang Y, Ye S, Chen J et al. A novel two-dimensional sparse MIMO array topology for UWB short-range imaging. IEEE Antennas and Wireless Propagation Letters 2015; 15: 702-705.

[13] Yanik ME, Torlak M. Near-field MIMO-SAR millimeter-wave imaging with sparsely sampled aperture data. IEEE Access 2019; 7: 31801-31819.

[14] Anadol E, Seker I, Camlica S, Topbas TO, Koc S et al. UWB 3D near-field imaging with a sparse MIMO antenna array for concealed weapon detection. In: SPIE Radar Sensor Technology XXII; Orlando, FL, USA; 2018. p. 106331D.

[15] Zhuge X, Yarovoy AG, Savelyev T, Ligthart L. Modified Kirchhoff migration for UWB MIMO array-based radar imaging. IEEE Transactions on Geoscience and Remote Sensing 2010; 48 (6): 2692-2703.

[16] Zhuge X, Yarovoy AG. Three-dimensional near-field MIMO array imaging using range migration techniques. IEEE Transactions on Image Processing 2012; 21 (6): 3026-3033.

[17] Lopez-Sanchez JM, Fortuny-Guasch J. 3-D radar imaging using range migration techniques. IEEE Transactions on Antennas and Propagation 2000; 48 (5): 728-737.

[18] Sakamoto T, Sato T, Aubry PJ, Yarovoy AG. Ultra-wideband radar imaging using a hybrid of Kirchhoff migration and Stolt FK migration with an inverse boundary scattering transform. IEEE Transactions on Antennas and Propagation 2015; 63 (8): 3502-3512.

[19] Tan K, Wu S, Liu X, Fang G. Omega-k algorithm for near-field 3-D image reconstruction based on planar SIMO/MIMO array. IEEE Transactions on Geoscience and Remote Sensing 2018; 57 (4): 2381-2394.

[20] Tan K, Wu S, Liu X, Fang G. A modified omega-k algorithm for near-field MIMO array-based 3-D reconstruction. IEEE Geoscience and Remote Sensing Letters 2018; 18 (99): 1-5.

[21] Álvarez Y, Rodriguez-Vaqueiro Y, Gonzalez-Valdes B, Las-Heras F, García-Pino A. Fourier-based imaging for subsampled multistatic arrays. IEEE Transactions on Antennas and Propagation 2016; 64 (6): 2557-2562.

[22] Candès EJ, Wakin MB. An introduction to compressive sampling. IEEE Signal Processing Magazine 2008; 25 (2): 21-30.

[23] Potter LC, Ertin E, Parker JT, Cetin M. Sparsity and compressed sensing in radar imaging. Proceedings of the IEEE 2010; 98 (6): 1006-1020.

[24] Ender JHG. On compressive sensing applied to radar. Signal Processing 2010; 90 (5): 1402-1414.

[25] Stojanovic I, Çetin M, Karl WC. Compressed sensing of monostatic and multistatic SAR. IEEE Geoscience and Remote Sensing Letters 2013; 10 (6): 1444-1448.

[26] Cheng Q, Alomainy A, Hao Y. Near-field millimeter-wave phased array imaging with compressive sensing. IEEE Access 2017; 5: 18975-18986.

[27] Tropp JA, Wright SJ. Computational methods for sparse solution of linear inverse problems. Proceedings of the IEEE 2010; 98 (6): 948-958.

[28] Samadi S, Çetin M, Masnadi-Shirazi MA. Sparse representation-based synthetic aperture radar imaging. IET Radar, Sonar & Navigation 2011; 5 (2): 182-193.

[29] Yang Z, Zheng YR. A comparative study of compressed sensing approaches for 3-D synthetic aperture radar image reconstruction. Digital Signal Processing 2014; 32: 24-33.

[30] Guo J, Zhang J, Yang K, Zhang B, Hong W et al. Information capacity and sampling ratios for compressed sensing-based SAR imaging. IEEE Geoscience and Remote Sensing Letters 2015; 12 (4): 900-904.

[31] Ma C, Yeo TS, Zhao Y, Feng J. MIMO radar 3D imaging based on combined amplitude and total variation cost function with sequential order one negative exponential form. IEEE Transactions on Image Processing 2014; 23 (5): 2168-2183.

[32] Guo L, Abbosh AM. Microwave stepped frequency head imaging using compressive sensing with limited number of frequency steps. IEEE Antennas and Wireless Propagation Letters 2015; 14: 1133-1136.

[33] Hu X, Tong N, Song B, Ding S, Zhao X. Joint sparsity-driven three-dimensional imaging method for multiple-input multiple-output radar with sparse antenna array. IET Radar, Sonar & Navigation.2016; 11 (5): 709-720.

[34] Ma C, Yeo TS, Ng BP. Multiple input multiple output radar imaging based on multidimensional linear equations and sparse signal recovery. IET Radar, Sonar & Navigation 2017; 12 (1): 3-10.

[35] Jiao Z, Ding C, Liang X, Chen L, Zhang F. Sparse Bayesian learning based three-dimensional imaging algorithm for off-grid air targets in MIMO radar array. Remote Sensing 2018; 10 (3): 369.

[36] Huang P, Li X, Wang H. Tensor-based match pursuit algorithm for MIMO radar imaging. Radio Engineering 2018; 27 (2): 581.

[37] Chen J, Li Y, Wang J, Li Y, Zhang Y. An accurate imaging algorithm for millimeter wave synthetic aperture imaging radiometer in near-field. Progress In Electromagnetics Research 2013; 141: 517-535.

[38] Gurbuz AC, McClellan JH, Scott WR Jr. Compressive sensing for subsurface imaging using ground penetrating radar. Signal Processing 2009; 89 (10): 1959-1972.

[39] Zhang W, Hoorfar A. A generalized approach for SAR and MIMO radar imaging of building interior targets with compressive sensing. IEEE Antennas and Wireless Propagation Letters 2015; 14: 1052-1055.

[40] Geman D, Yang C. Nonlinear image recovery with half-quadratic regularization. IEEE Transactions on Image Processing 1995; 4 (7): 932-946.

[41] Vogel CR, Oman ME. Fast, robust total variation-based reconstruction of noisy, blurred images. IEEE Transactions on Image Processing 1998; 7 (6): 813-824.

[42] Kocamis MB, Oktem FS. Optimal design of sparse MIMO arrays for near-field ultrawideband imaging. In: 2017 25th European Signal Processing Conference; Kos, Greece; 2017. pp. 1952-1956.

[43] Beck A, Teboulle M. Gradient-based algorithms with applications to signal recovery. In: Palomar DP, Eldar YC (editors). Convex Optimization in Signal Processing and Communications. New York, NY, USA: Cambridge University Press, 2010, pp. 42-88.

[44] Oktem FS, Gao L, Kamalabadi F. Computational spectral and ultrafast imaging via convex optimization. In: Monga V (editor). Handbook of Convex Optimization Methods in Imaging Science. Cham, Switzerland: Springer, 2018, pp. 105-127.